Evidence for $Cu_{2-x}Se$ platelets at grain boundaries and within grains in $Cu(In,Ga)Se_2$ thin films

E. Simsek Sanli, Q. M. Ramasse, R. Mainz, A. Weber, D. Abou-Ras, W. Sigle, and P. A. van Aken

Citation: Appl. Phys. Lett. **111**, 032103 (2017); doi: 10.1063/1.4993917
View online: https://doi.org/10.1063/1.4993917
View Table of Contents: http://aip.scitation.org/toc/apl/111/3
Published by the American Institute of Physics

APPLIED PHYSICS LETTERS **111**, 032103 (2017)

Evidence for $Cu_{2-x}Se$ platelets at grain boundaries and within grains in $Cu(In,Ga)Se_2$ thin films

E. Simsek Sanli,[1,a)] Q. M. Ramasse,[2] R. Mainz,[3] A. Weber,[3] D. Abou-Ras,[3] W. Sigle,[1] and P. A. van Aken[1]
[1]*Stuttgart Center for Electron Microscopy, Max Planck Institute for Solid State Research, Heisenbergstr. 1, 70569 Stuttgart, Germany*
[2]*SuperSTEM Laboratory, SciTech Daresbury Campus, Keckwick Lane, Daresbury WA4 4AD, United Kingdom*
[3]*Helmholtz–Zentrum Berlin für Materialien und Energie GmbH, Hahn-Meitner-Platz 1, 14109 Berlin, Germany*

(Received 14 May 2017; accepted 1 July 2017; published online 18 July 2017)

$Cu(In,Ga)Se_2$ (CIGS)-based solar cells reach high power-conversion efficiencies of above 22%. In this work, a three-stage co-evaporation method was used for their fabrication. During the growth stages, the stoichiometry of the absorbers changes from Cu-poor ($[Cu]/([In] + [Ga]) < 1$) to Cu-rich ($[Cu]/([In] + [Ga]) > 1$) and finally becomes Cu-poor again when the growth process is completed. It is known that, according to the Cu-In-Ga-Se phase diagram, a Cu-rich growth leads to the presence of $Cu_{2-x}Se$ ($x = 0$–0.25), which is assumed to assist in recrystallization, grain growth, and defect annihilation in the CIGS layer. So far, $Cu_{2-x}Se$ precipitates with spatial extensions on the order of 10–100 nm have been detected only in Cu-rich CIGS layers. In the present work, we report $Cu_{2-x}Se$ platelets with widths of only a few atomic planes at grain boundaries and as inclusions within grains in a polycrystalline, Cu-poor CIGS layer, as evidenced by high-resolution scanning transmission electron microscopy (STEM). The chemistry of the Cu–Se secondary phase was analyzed by electron energy-loss spectroscopy, and STEM image simulation confirmed the identification of the detected phase. These results represent additional experimental evidence for the proposed topotactical growth model for Cu–Se–assisted CIGS thin-film formation under Cu-rich conditions.
[http://dx.doi.org/10.1063/1.4993917]

A multi-stage co-evaporation technique is used for the fabrication of $Cu(In,Ga)Se_2$ (CIGS) absorbers for high-efficiency thin-film solar cells.[1] In this technique, the CIGS absorbers pass through a Cu-rich ($[Cu]/([In] + [Ga]) > 1$) stoichiometry, which is essential for recrystallization, grain growth, and defect annihilation and finally for better crystal quality.[2–4] However, a Cu-rich stoichiometry is known to lead to the formation of a secondary phase, $Cu_{2-x}Se$ ($x = 0$–0.25), at the absorber surface and at grain boundaries (GBs) within the film.[5–7] The secondary phase formed at the surface can be removed by chemical treatments (NaCN, KCN, etc.) for thermal co-evaporation or two-stage processes.[5,6,8] For three-stage processes, the secondary phase is thought to be consumed during the third stage by simultaneous In, Ga, and Se deposition. The third stage also leads to higher efficiencies by reducing the Cu amount ($[Cu]/[In] + [Ga] < 1$) of the CIGS absorber.

The detection of secondary phases in the CIGS system by X-ray diffraction and transmission electron microscopy (TEM) imaging in combination with energy-dispersive X-ray spectroscopy initiated research on the growth mechanisms for ternary $CuInSe_2$ (CIS) and $CuGaSe_2$ (CGS) and quaternary CIGS thin-films. In 1993, Klenk *et al.* proposed a vapor–liquid–solid mechanism as a growth model for large-grained CIS and CGS films under Cu-rich conditions.[9] In 1997, Wada *et al.* proposed a different growth model called "topotactic reaction" for CIS.[10] A topotactic reaction is a chemical solid-state reaction, where the initial and final crystals have a three-dimensional crystallographic relation.[11] In later work, Nishiwaki *et al.* explained the growth of CIGS produced by the three-stage co-evaporation technique with the same model.[12] According to their proposed model, during the third stage of this process, two reactions occur: (i) the growth of CIGS grains from the $Cu_{2-x}Se$ phase through the incorporation of In and Ga and in the presence of sufficiently high Se vapor pressure. The $Cu_{2-x}Se$ phase is thought to transform to CIGS by maintaining the Se sublattice in the same cubic closed-packed structure, while the cations are being exchanged. The crystallographic relation between the pseudo-cubic CIGS and the cubic $Cu_{2-x}Se$ is given by Wada *et al.* as follows: $(11\bar{1})_{Cu2Se} \| (11\bar{1})_{CIS}$ and $[011]_{Cu2Se} \| [011]_{CIS}$;[10] (ii) the decomposition of CIGS and the formation of indium selenide and gallium selenide. However, this second (clearly unwanted) reaction can be impeded by sufficient Se flux or even be reversed without any decomposition of the forming CIGS.[12]

In previous studies, the detected $Cu_{2-x}Se$ phases extended spatially up to several hundred nm and were only found in Cu-rich ternary and quaternary absorbers. In this study, we detected in a Cu-poor CIGS absorber $Cu_{2-x}Se$ platelets with widths of a few atomic planes by high-resolution scanning TEM (HR-STEM). We analyzed the chemical composition of the detected phase *via* electron energy-loss spectroscopy (EELS). We then combined chalcopyrite CIS and cubic Cu_2Se crystal structures to build a defect model informed by

---

[a)] Author to whom correspondence should be addressed: e.simsek@fkf.mpg.de

the atomic-scale observations. Finally, we used this model for image simulations using the Quantitative TEM/STEM Simulations software suite (QSTEM)[13] in order to confirm the identification of the structure of platelets within the grains. The observation of remnants of the $Cu_{2-x}Se$ phase in the Cu-poor CIGS matrix gives an atomic-scale and direct experimental evidence for the topotactical growth model of CIGS absorber layers produced by a three-stage co-evaporation process.

The CIGS absorber layer studied here was grown by three-stage co-evaporation of all the elements on Mo-coated, soda-lime glass at low temperatures, starting with 330 °C at the first stage and continuing with 430 °C as a maximum substrate temperature during the second and third stages. The absorber layer reached the desired Cu-poor composition ([Cu]/([In] + [Ga]) ~ 0.8) at the end of the third stage. The samples were prepared for the HR-STEM measurements by a focused ion beam (FIB) using a Zeiss Crossbeam XB 1540 EsB instrument and applying an in-situ lift-out method.[14] HR-STEM measurements were carried out at 100 kV on a Nion UltraSTEM 100 microscope, equipped with a cold field-emission source and a C_s probe corrector. The beam semi-convergence angle was 33 mrad for imaging, and the semi-collection angle was 38 mrad for the EELS measurements. The high-angle annular dark-field (HAADF) detector's angular range was 85–185 mrad for HR-STEM imaging. A Gatan Enfina spectrometer was used for the EELS measurements, and the energy-loss range was set from 315 eV to 1655 eV to allow the simultaneous elemental mapping of all the film's constituents by using In-$M_{4,5}$, Cu-$L_{2,3}$, Ga-$L_{2,3}$, and Se-$L_{2,3}$ ionization edges. The EEL spectra were processed using the Multivariate Statistical Analysis (MSA) plug-in for Gatan Digital Micrograph, based on weighted principal component analysis (PCA), to reduce noise.[15]

Figure 1(a) shows two grains, where the upper grain is oriented in the ⟨110⟩-direction and the bottom grain is oriented in an unknown direction. A lower magnification image can be found in the supplementary material (Fig. S1). These two grains are separated by about 5 atomic planes forming a platelet coherently grown on the upper grain. The platelet exhibits a clearly different crystal structure from the upper grain as shown in Fig. 1(a). In the ⟨110⟩-projection of the CIGS structure, Se and cation (Cu, In, and Ga) columns are closely spaced and form a characteristic dumbbell structure, whereas the platelet exhibits triplets of closely spaced Cu-Se-Cu atomic columns instead. Cu, In, and Se elemental maps [Figs. 1(b)–1(d)] extracted from the EEL spectrum image acquired from the region indicated with a green box in Fig. 1(a) show the chemical differences between the CIGS matrix and the platelet present at the GB: the platelet is richer in Cu than the main grain, while the concentration of In is strongly depleted. The platelet is therefore identified as $Cu_{2-x}Se$. It should be mentioned that the In and Ga concentrations vary across the absorber layer—as is explained in more detail in a previous study.[16] In the present study, the middle part of the sample, where we detected the secondary phase, was Ga-poor. Therefore, no Ga elemental distribution map is shown here as almost no Ga signal was detected in the experimental data. Figure 1(e) shows a composite image formed by overlapping a simultaneous HAADF image, acquired during spectrum image acquisition, and a red–green–blue (RGB) composite image, showing the distribution of Se, Cu, and In, respectively. The interplanar distances for the Se columns are equal for both the CIGS matrix and the $Cu_{2-x}Se$ phase. The $Cu_{2-x}Se$ phase seems highly ordered, although the EELS map suggests a somewhat smeared Cu distribution in the ⟨110⟩-direction which can be attributed to the close positioning of Cu columns in that direction. The slightly lowered Se signal intensity around the GB region gives further credence to the identification of a secondary phase different from the bulk, going from a high Se concentration CIGS matrix to the lower Se concentration $Cu_{2-x}Se$ phase. In previous studies, the occurrence of cation redistribution at random GBs was unambiguously demonstrated, including clear evidence for regions with Cu enrichment and In depletion.[16,17] However, contrary to the present report, these Cu-rich/In-poor boundary regions did not exhibit any clear crystallinity, i.e., no highly ordered secondary phase was observed at those boundaries. The presence of a remnant $Cu_{2-x}Se$ fully ordered phase at GBs and within grains appears therefore to be a rare occurrence (within the limited statistics of atomic-resolution STEM observation).

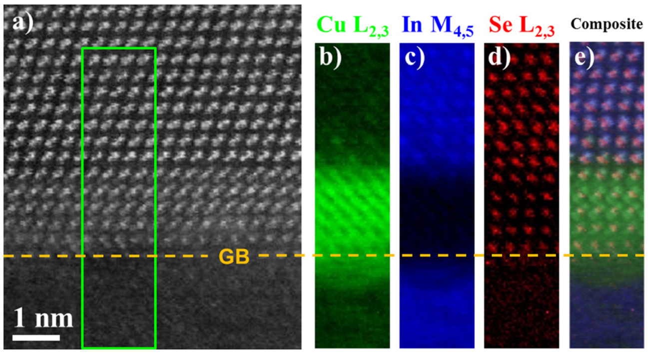

FIG. 1. (a) $Cu_{2-x}Se$ platelet around a grain boundary (GB) on {112} planes. Elemental distribution maps of (b) Cu-$L_{2,3}$, (c) In-$M_{4,5}$, and (d) Se-$L_{2,3}$ are extracted from the acquired EEL spectrum image. (e) Simultaneous HAADF image and a red-green-blue (RGB) composite image are superimposed. The CIGS dumbbell structure and the $Cu_{2-x}Se$ platelet are clearly visible.

We also detected the same coherent structure identified as the $Cu_{2-x}Se$ platelet within the CIGS grain, similarly aligned along the {112} planes. Figure 2(a) shows an example of a platelet inclusion consisting of three atomic planes of $Cu_{2-x}Se$ within the CIGS matrix. A lower magnification image of the platelet and a similar example of a platelet with two atomic planes of the $Cu_{2-x}Se$ phase are shown in Figs. S2 and S3, respectively, in the supplementary material. Figures 2(b)–2(d) show Cu, In, and Se elemental maps extracted from the EEL spectrum image acquired across the region indicated by a green box in Fig. 2(a). The composite image [Fig. 2(e)] shows a polarity inversion of the Se and cation columns in the CIGS matrix across the $Cu_{2-x}Se$ platelet: the red Se atomic columns are on the down-side of the dumbbells in the upper part of the matrix but on the top-side of the dumbbells in the bottom side of the CIGS matrix. The reason for this site reversal is the presence of additional Cu columns in the $Cu_{2-x}Se$ phase. As was the case at the GB, the Se map shows the uninterrupted continuation of the Se sub-lattice, whereas Cu and In cations are exchanged. This is

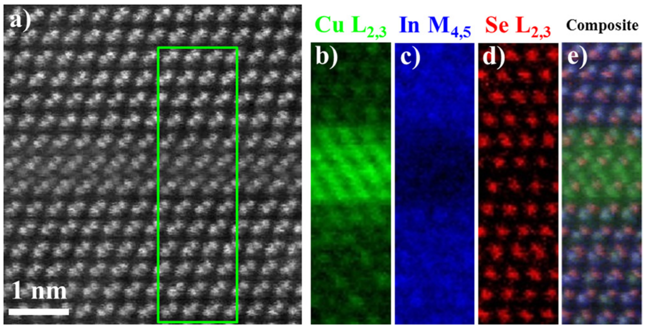

FIG. 2. (a) $Cu_{2-x}Se$ platelet in the CIGS phase on {112} planes. Elemental distribution maps of (b) Cu-$L_{2,3}$, (c) In-$M_{4,5}$, and (d) Se-$L_{2,3}$ are extracted from the acquired EEL spectrum image. (e) Simultaneous HAADF image is superimposed to a RGB composite image that shows the Se, Cu, and In elemental distributions.

the clearest experimental evidence to date for the topotactical growth model of CIGS under Cu-rich conditions.

Despite its simple binary chemical formula, copper selenide forms complex stoichiometric (CuSe, Cu_2Se, $CuSe_2$, and Cu_3Se_2) and non-stoichiometric ($Cu_{2-x}Se$) phases.[18,19] There are two main equilibrium phases for the non-stoichiometric $Cu_{2-x}Se$ phase at lower Cu concentrations: a high temperature β-$Cu_{2-x}Se$ phase and a low temperature α-$Cu_{2-x}Se$ phase.[20] It has also been noted that for $x = 0.15$–0.25, the high temperature phase can be present at room temperature.[21] While the STEM-EELS results unequivocally show the presence of a secondary $Cu_{2-x}Se$ phase, a comparison of the structure observed experimentally with simulations can help to confirm the specific crystallography of the inclusion phase. Thus, in order to validate the experimental observations, a model structure was created, informed by the experimental images of the platelets incorporated within a CIS matrix (no Ga ions were included in the model structure for simplicity due to the low Ga content in the region of the film observed experimentally). A chalcopyrite-type crystal structure was used for the CIS. The chalcopyrite structure is a tetragonal structure with the space group $I\bar{4}2d$. In the chalcopyrite structure, the Cu atoms sit on the 4a (000) and In cations are on 4b ($00\frac{1}{2}$) positions, and they are tetrahedrally coordinated to Se on the 8d ($0\frac{1}{4}\frac{1}{8}$) positions. An anti-fluorite type structure with the space group $Fm\bar{3}m$ was used for the $Cu_{2-x}Se$ platelet, as the most likely structure, following Wada *et al.*[10] In the parent stoichiometric Cu_2Se structure (used in the model for simplicity, as an unambiguous determination of the exact platelet stoichiometry through EELS would be difficult), 4 Se atoms form a simple fcc sublattice, 4a (000), with 8 Cu atoms occupying the interstitial tetrahedral and octahedral sites, 8c ($\frac{1}{4}\frac{1}{4}\frac{1}{4}$), in the subcell.[18] The lattice parameters are adapted to match with the surrounding CIS to $a = 5.8$ Å and $c = 11.6$ Å and with Cu_2Se to $a = 5.8$ Å. Figures 3(a) and 3(b) show a ⟨110⟩-projection of the created CIS and Cu_2Se crystal structures visualized using Vesta.[22] The incorporation of a Cu_2Se platelet within a CIS matrix [Fig. 3(c)] with 23 nm thickness was carried out using Model Builder, a complex interface building tool provided in the QSTEM software suite, which is a free image simulation software based on frozen phonon multislice methods.[13] The simulation parameters were chosen to reflect the experimental conditions: 100 kV acceleration voltage with a semi-convergence angle of 33 mrad, and the HAADF detector's semi-angles were set to 85–190 mrad. Figure 3(d) shows a simulated image for a total sample thickness of 16.1 nm, chosen to match with the measured thickness of the FIB lamella (∼15 nm). The simulation is shown in the yellow frame overlaid on top of an experimental image, obtained by rigid-registration of a series of rapidly scanned HAADF images.[23]

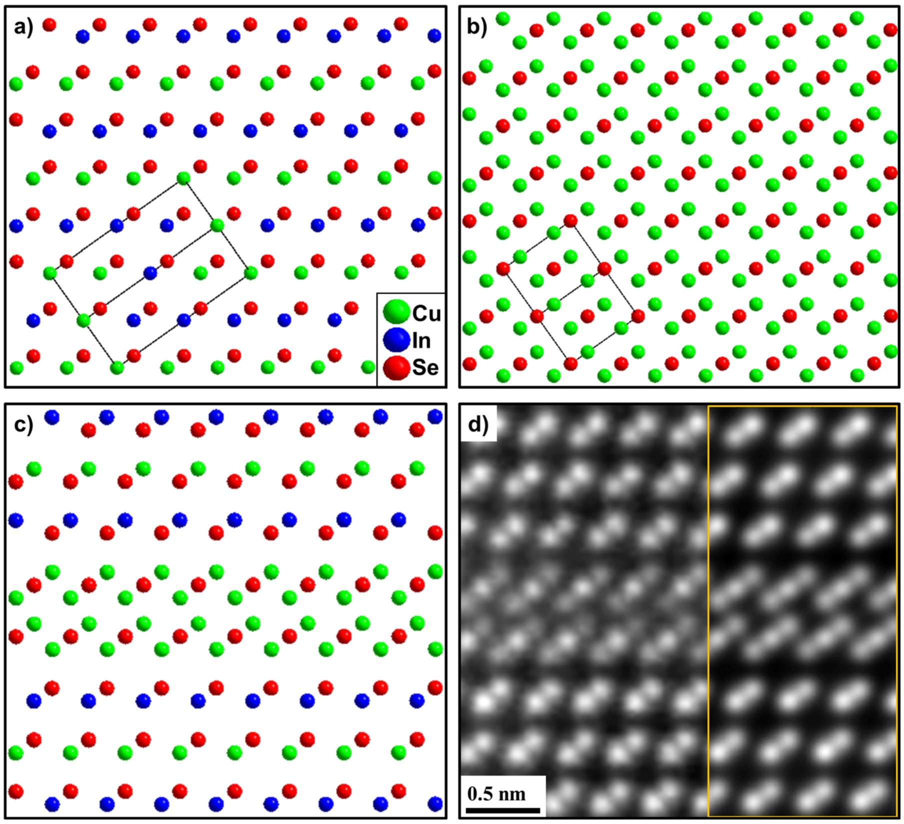

FIG. 3. ⟨110⟩-projection of the created (a) CIS—with a chalcopyrite crystal structure—and (b) Cu_2Se—with an anti-fluorite crystal structure—based on the study by Wada *et al.*[10] The unit cells are shown with black frames on the crystal structures. (c) Simulated model of $Cu_{2-x}Se$ in the CIS matrix. (d) Averaged sequential image overlapped with the simulated model of $Cu_{2-x}Se$ in the CIS matrix.

The intensities in the simulated image and real image show an excellent match. We note however that the comparison is not provided on an absolute intensity scale: the intensities of both simulated and experimental images were stretched to the full greyscale range. Although the simulation is therefore not fully quantitative, it certainly demonstrates a good structural agreement with the proposed anti-fluorite phase. Other possible crystal structures were also considered: aside from the anti-fluorite structure used above, the other most likely Cu-Se containing secondary phases are $F\bar{4}3m$ and $F23$ for Cu_2Se and $Pnmm$ for $CuSe_2$. Models of these structures are presented in Fig. S4 (supplementary material) for completeness. However, a cursory visual inspection of these models clearly demonstrates a poor match to the observed HAADF images, and full simulations were therefore not attempted.

In conclusion, we provide direct experimental evidence for the presence of a secondary $Cu_{2-x}Se$ phase by HR-STEM and EELS in a Cu-poor CIGS absorber layer grown *via* a three-stage co-evaporation process. The $Cu_{2-x}Se$ phase is shown to form platelets that are aligned with parallel to the {112} planes of the CIGS chalcopyrite structure. The platelets are a few atomic planes in width and are found at GBs but also as inclusions within the grains of the Cu-poor CIGS. The identification of the $Cu_{2-x}Se$ phase, as the same anti-fluorite structure proposed by Wada *et al.*[10] in the case of Cu-rich CIS absorbers, was confirmed by means of comparison to image simulations of a model structure derived from the experimental observations. The observation of these platelets, which are likely the remnants of the $Cu_{2-x}Se$ phase known to form during the Cu-rich phase of the growth, in particular, as small inclusions within grains, provides the most direct and conclusive experimental evidence to date of the proposed topotactical growth model for the formation of CIGS absorbers produced by the three-stage co-evaporation technique.

See supplementary material for lower magnification images of platelets, the STEM-EELS analysis of a platelet with two atomic planes of the $Cu_{2-x}Se$ phase in the CIGS grain, and the models of most likely Cu-Se containing secondary phases.

The authors thank Dr. Bernhard Fenk for FIB sample preparation. This work was supported in part by the Helmholtz Virtual Institute HVI–520 "Microstructure Control for Thin-Film Solar Cells", by the European Union Seventh Framework Program [FP/2007–2013] under Grant Agreement No. 312483 (ESTEEM2), and by the European Metrology Research Programme (EMRP) Project IND07 Thin Films. The EMRP is jointly funded by the EMRP participating countries within EURAMET and the European Union. SuperSTEM is the UK National Facility for Aberration-Corrected STEM, funded by EPSRC.

[1] A. M. Gabor, J. R. Tuttle, D. S. Albin, M. A. Contreras, R. Noufi, and A. M. Hermann, Appl. Phys. Lett. **65**(2), 198 (1994).
[2] R. Mainz, E. Simsek Sanli, H. Stange, D. Azulay, S. Brunken, D. Greiner, S. Hajaj, M. D. Heinemann, C. A. Kaufmann, M. Klaus, Q. M. Ramasse, H. Rodriguez-Alvarez, A. Weber, I. Balberg, O. Millo, P. A. van Aken, and D. Abou-Ras, Energy Environ. Sci. **9**(5), 1818 (2016).
[3] J. K. Larsen, L. Gütay, and S. Siebentritt, Appl. Phys. Lett. **98**(20), 201910 (2011).
[4] R. Caballero, C. A. Kaufmann, V. Efimova, T. Rissom, V. Hoffmann, and H. W. Schock, Prog. Photovoltaics **21**(1), 30 (2013).
[5] J. R. Tuttle, D. S. Albin, and R. Noufi, Sol. Cells **27**(1), 231 (1989).
[6] V. Nadenau, D. Hariskos, H.-W. Schock, M. Krejci, F.-J. Haug, A. N. Tiwari, H. Zogg, and G. Kostorz, J. Appl. Phys. **85**(1), 534 (1999).
[7] Y. Yan, K. M. Jones, J. AbuShama, M. M. Al-Jassim, and R. Noufi, MRS Online Proc. Library **668**, H6.10.1 (2001).
[8] J. R. Tuttle, D. S. Albin, and R. Noufi, Sol. Cells **30**(1), 21 (1991).
[9] R. Klenk, T. Walter, H.-W. Schock, and D. Cahen, Adv. Mater. **5**(2), 114 (1993).
[10] T. Wada, N. Kohara, T. Negami, and M. Nishitani, J. Mater. Res. **12**(6), 1456 (1997).
[11] U. Müller, *Symmetry Relationships between Crystal Structures: Applications of Crystallographic Group Theory in Crystal Chemistry* (OUP Oxford, 2013).
[12] S. Nishiwaki, N. Kohara, T. Negami, H. Miyake, and T. Wada, Jpn. J. Appl. Phys., Part 1 **38**(5R), 2888 (1999).
[13] C. T. Koch, "Determination of core structure periodicity and point defect density along dislocations," Ph.D. thesis (Arizona State University, 2002).
[14] M. H. F. Overwijk, F. C. van den Heuvel, and C. W. T. Bulle-Lieuwma, J. Vac. Sci. Technol. B **11**(6), 2021 (1993).
[15] E. O. Masashi Watanabe and K. Ishizuka, Microsc. Anal. **23**(7), 5 (2009).
[16] E. Simsek Sanli, Q. M. Ramasse, W. Sigle, D. Abou-Ras, R. Mainz, A. Weber, H.-J. Kleebe, and P. A. van Aken, J. Appl. Phys. **120**(20), 205301 (2016).
[17] D. Abou-Ras, B. Schaffer, M. Schaffer, S. S. Schmidt, R. Caballero, and T. Unold, Phys. Rev. Lett. **108**(7), 075502 (2012).
[18] D. J. Chakrabarti and D. E. Laughlin, Bull. Alloy Phase Diagrams **2**(3), 305 (1981).
[19] S. R. Gosavi, N. G. Deshpande, Y. G. Gudage, and R. Sharma, J. Alloys Compd. **448**(1–2), 344 (2008).
[20] H. Liu, X. Shi, F. Xu, L. Zhang, W. Zhang, L. Chen, Q. Li, C. Uher, T. Day, and G. J. Snyder, Nat. Mater. **11**(5), 422 (2012).
[21] N. H. Abrikosov, V. F. Bankina, M. A. Korzhuev, G. K. Demski, and O. A. Teplov, Sov. Phys. Solid State **25**, 1678 (1983).
[22] K. Momma and F. Izumi, J. Appl. Crystallogr. **44**(6), 1272 (2011).
[23] K. Kimoto, T. Asaka, X. Yu, T. Nagai, Y. Matsui, and K. Ishizuka, Ultramicroscopy **110**(7), 778 (2010).